

Finding synchronization state of higher-order motif networks by dynamic learning

Zhiqiu Ye, Yong Wu, Qianming Ding, Ying Xie, and Ya Jia ^{*}

Department of Physics and Institute of Biophysics, Central China Normal University, Wuhan 430079, China

 (Received 30 April 2024; accepted 4 July 2024; published 15 July 2024)

Synchronization of action potentials is one of the important phenomena for neural networks to achieve biological functions. How to find the optimal parameter space of neural networks in a synchronized state is of great significance for studying their synchronization. This study explores the parameter space of triplet motif-based higher-order networks in a synchronized state through the dynamic learning of synchronization (DLS) technique, which dynamically modulates the connection weights between motifs to alter their firing patterns. Our study delves into regular, Erdős-Rényi random graphs, small-world, and scale-free networks, emphasizing the high-order motif interactions that characterize these networks. Our key findings indicate that the DLS technique successfully promotes synchronization within high-order motif networks with various connection patterns, although the degree of synchronization in networks where motifs are interconnected by chemical synapses is slightly weaker than those interconnected by electrical synapses. Additionally, we demonstrate the pattern of weight changes during the regulation of network firing states by DLS, finding that the evolution of weight distributions correlates with the network's topological structure. This work might provide new insights into complex network synchronization and lays the foundation for further exploration of using DLS technology to synchronize higher-order networks through external factors.

DOI: [10.1103/PhysRevResearch.6.033071](https://doi.org/10.1103/PhysRevResearch.6.033071)

I. INTRODUCTION

Billions of neurons in the human brain are interconnected through synapses, working together to form neural networks with complex dynamics [1,2]. Synchronization is a key phenomenon in the dynamic activities of neural networks, characterized by the temporal coordination of firing states among different neurons [3–5]. Through such dynamic behaviors, neurons can efficiently transmit information, thereby facilitating cognitive processes and other functional operations [6–8]. Neurons can form specific connection patterns known as motifs, with the motif composed of three neurons being the most common type [9]. These motifs, as higher-order structures, exhibit complex dynamic properties within the network [10–12]. Synchronization within these motifs is crucial [13–15]. The transitions in synchronization patterns can enhance the influence of feedback mechanisms in the nervous system. Research into motif synchronization not only helps reveal fundamental brain mechanisms but also has profound implications for treating neurological diseases (such as epilepsy [16] and Parkinson's disease [17]) and for developing bio-inspired computing [18,19]. Therefore, a deeper exploration of synchronization phenomena in high-order

motif networks can significantly improve our understanding of the brain's complex functions.

The local network of the brain cortex can be viewed as a skeleton composed of stronger connections within a sea of weaker ones [20]. This motif network structure is widely considered an essential tool for analyzing complex networks [21]. In motif networks, the factors influencing synchronization have been extensively studied. Lizier *et al.* analyzed how the connection patterns within motifs affect the overall network's synchrony, revealing that feed-forward and feedback loop structures are key elements in regulating synchrony [22]. Additionally, the stability of synchronization in motif networks is closely related to the network topological structure, primarily depending on two critical topological characteristics of the network [23]. By adjusting the topology of the motif network, synchronization states can be effectively (de)stabilized, thus controlling the overall behavior of the network.

Although existing researches provide significant insights into the synchrony of networks [24–26], they often rely on prior experience and complex parameter adjustments [27,28]. This reliance limits the application of such research to broader real-world scenarios, especially in rapidly changing environments. Consequently, two critical questions arise: Can the optimal synchronization parameters for motif networks be quickly identified without prior experience? And, can the network quickly recover to a synchronized state after an external attack? Here, “optimal synchronization parameters” refer to those parameters that ensure the network can achieve and maintain synchronization in a stable, efficient, and robust manner. To address these issues, dynamic learning of synchronization (DLS) technology has recently been proposed [29]. This technique employs innovative strategies to capture

^{*}Contact author: jiay@ccnu.edu.cn

Published by the American Physical Society under the terms of the Creative Commons Attribution 4.0 International license. Further distribution of this work must maintain attribution to the author(s) and the published article's title, journal citation, and DOI.

the differences in membrane potentials across the network's nodes, dynamically adjusting network parameters. A recent study has shown that DLS can also flexibly modulate external stimuli through real-time monitoring of network status, significantly enhancing the network's ability to adapt to environmental changes and resist external disturbances [30]. Analyzing the effects of DLS technique in various application scenarios [30,31], offers a fresh perspective on synchronization research, contributing to a deeper understanding of the mechanisms regulating synchronization in complex networks.

Compared to other complex networks, high-order motif networks exhibit interactions both within and between motifs, making their dynamic properties more complex and their synchronization studies more challenging [32,33]. Parastesh *et al.* analyzed the cost of synchronization in high-order networks, finding that second-order interactions achieve synchronization more easily than first-order interactions [34]. Additionally, research on how high-order networks balance different types of interactions has shown that as the interactions equitably strengthen, so does the collective synchronization behavior of the network [35]. However, studies on the impact of dynamic conditions such as weight changes and noise fluctuations between motifs on the synchronization of high-order motif networks remain insufficient.

In order to explore the adaptive synchronization of high-order networks, we construct a high-order network composed of triplet motifs, using the Hodgkin-Huxley model [36] as the base node. When the network state changes dynamically or the network is attacked, DLS technology is applied to modulate the weights between motifs. This allows for testing the network's potential to achieve synchronization in a dynamic environment without prior experience. The study also analyzes the pattern of weight changes between motifs throughout the dynamic learning process. Discussing the regulatory effect of DLS technology on the synchronization of high-order motif networks not only deepens the understanding of synchronization mechanisms in high-order networks but also provides new insights for achieving effective synchronization control in similar networks.

The subsequent content of this study is organized as follows. Section II provides a detailed description of the setup of triplet motif-based high-order network, the dynamic learning of synchronization technique, and the statistical measures used. Section III tests the firing state of the high-order motif network through numerical simulation. Using measures like the synchronization factor, we examine the dynamics of higher-order networks under the influence of external factors such as connection weights and noise fluctuations. Additionally, we explore the changes in weight parameters during synchronization modulation process. Section IV presents the conclusions of this study.

II. MODEL AND METHOD

A. Higher-order motif network structure

We consider a high-order network of triplet neuron motifs [37], each node in the network represents a motif composed of three neurons, which is one of the most important structures in the brain [20]. A schematic diagram of the network and

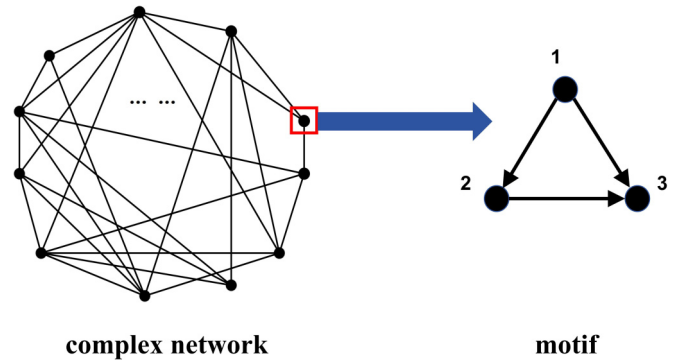


FIG. 1. Schematic representation of a higher-order motif network and its neuronal components. Within the complex network, each node is composed of a triplet of HH neurons, forming a basic motif. In the motif, each black dot signifies an individual HH neuron. Connections between neurons are illustrated by black arrows, and all intramotif connections are directed. All neurons within this networked motif are subject to the influence of an external stimulating current. For simplicity, within each motif, Neuron 3 is designated as the signal output unit to establish connections with neurons in other motifs within the network.

motif connections is shown in Fig. 1. We discussed four types of topological structures: fully connected (FC), Erdős-Rényi (ER) random graphs [38], small-world (SW) [39], and scale-free (SF) [40] networks. The HH model was used to simulate the membrane potential of each neuron node and the variation of gating and other variables. The dynamics of a single neuron takes the following form:

$$\begin{aligned}
 C_m \frac{dV_i}{dt} &= -I_{Na}^i - I_K^i - I_L^i + I_{ext}^i + I_{syn_1}^i + I_{syn_2}^i + \xi_i(t), \\
 I_{Na}^i &= g_{Na} m_i^3 h_i (V_i - V_{Na}), \\
 I_K^i &= g_K n_i^4 (V_i - V_K), \\
 I_L^i &= g_L (V_i - V_L),
 \end{aligned} \tag{1}$$

where V_i is the membrane potentials in i th motif of the network, which include V_{i_1} , V_{i_2} , and V_{i_3} representing the membrane potentials of node 1, node 2, and node 3 in the i th motif, respectively. The subscript i (where $i = 1, 2, \dots, N$) indexes the sequence of motif networks in the equations, with N being the total number of motifs in the network. In the simulations, N is set to 100. C_m is the membrane capacitance per unit area of the neuron, fixed to 1 $\mu\text{F}/\text{cm}^2$. The applied external current was set to a normal distribution with center of distribution $I_{ext} = 10 \mu\text{A}/\text{cm}^2$. Maximum conductance of ion channels in the model are $g_K = 36 \text{ mS}/\text{cm}^2$, $g_{Na} = 120 \text{ mS}/\text{cm}^2$, and $g_L = 0.3 \text{ mS}/\text{cm}^2$. The reverse potential of each ion channel is: $V_K = -77 \text{ mV}$, $V_{Na} = 50 \text{ mV}$, and $E_L = -54.4 \text{ mV}$. In contrast to the original paper, this study associated the reversal potential with resting potential $V_{rest} \approx -65 \text{ mV}$. For a more detailed explanation of these parameters, further information can be found in the original paper [1]. In the higher-order motif network, each node is also subjected to noise disturbances. In Eq. (1), $\xi_i(t)$ represents Gaussian white noise, with statistical properties given by $\langle \xi_i(t) \rangle = 0$, and the

autocorrelation $\langle \xi_i(t)\xi_i(t') \rangle = 2D\delta(t-t')$, where $\delta(t)$ is the Dirac delta function, and D denotes the noise intensity.

n_i , m_i , and h_i are the gating variables of ionic channels in the model, which are represented as follows:

$$\frac{dx_i}{dt} = \alpha_{x_i}(V_i)(1-x_i) - \beta_{x_i}(V_i)x_i, \quad (x = n, m, h), \quad (2)$$

where the α_{x_i} and β_{x_i} are the channel conversion rates, they are described by:

$$\begin{aligned} \alpha_{n_i} &= \frac{0.01(V_i + 55)}{1 - \exp[-(V_i + 55)/10]}, \\ \beta_{n_i} &= 0.125\exp(-(V_i + 65)/80), \\ \alpha_{m_i} &= \frac{0.1(V_i + 40)}{1 - \exp[-(V_i + 40)/10]}, \\ \beta_{m_i} &= 4\exp(-(V_i + 65)/18), \\ \alpha_{h_i} &= 0.07\exp(-(V_i + 65)/20), \\ \beta_{h_i} &= \frac{1}{1 + \exp[-(V_i + 35)/10]}. \end{aligned} \quad (3)$$

Regarding the connectivity within each motif of the network, Fig. 1 illustrates that synaptic coupling directions are represented by arrowheads; specifically, neuron 1 drives neuron 2, which in turn, along with neuron 1, impacts neuron 3. Neuron 3 is designated as the output neuron for each motif. This designation simplifies the model by allowing the output neuron 3 of each motif to form connections with neurons in other motifs throughout the network. Synaptic connections within the motifs are mediated via chemical synapses. In this work, the modeling of chemical synaptic coupling is achieved using the α function. The synaptic current received by neuron i from within its own motif, denoted by I_{syn_i} , and α function are mathematically represented as follows:

$$\begin{aligned} I_{\text{syn}_i}^i &= \sum G\varepsilon(t - t_{\text{pre}})(V_{\text{syn}} - V_i), \\ \alpha(t) &= \frac{t}{\tau_{\text{syn}}} \exp\left(-\frac{t}{\tau_{\text{syn}}}\right)\Theta(t), \end{aligned} \quad (4)$$

where G is the coupling strength. For simplicity, we assume uniform coupling strengths within the motif. The connection matrix ε signifies the connection type within the motif, as illustrated in Fig. 1. Here, t_{pre} represents the most recent firing time of the presynaptic neuron in the motif before time t . V_{syn} stands for the synaptic reversal potential, set to 0 mV for all neurons are considered as excitatory type in this study. $\Theta(t)$ is the Heaviside function.

In the context of complex networks, connections between neurons that are bridged by electrical and chemical synapses across disparate motifs are considered separately. The corresponding coupled currents are formulated as follows:

$$I_{\text{syn}_2}^i = \sum_j^N \delta_{ij}g_{ij}(V_i), \quad (5)$$

where w_{ij} is connectivity weight and δ_{ij} is the connection matrix. The connection equation, denoted as $g_{ij}(\ast)$, encompasses both electrical synapse and chemical synapse. Specifically,

electrical synapse can be succinctly expressed as follows:

$$g_{e,ij} = \delta_{ij}(V_j - V_i), \quad (6)$$

and the modeling of chemical synaptic coupling also employs the α function:

$$\begin{aligned} g_{\text{syn},ij} &= \alpha(t - t_j)(V_{\text{syn}} - V_i), \\ \alpha(t) &= \frac{t}{\tau_{\text{syn}}} \exp\left(-\frac{t}{\tau_{\text{syn}}}\right)\Theta(t). \end{aligned} \quad (7)$$

B. Dynamic learning of synchronization technique

The dynamics of nonlinear systems characterized by coupling behaviors can be effectively summarized using dynamic expressions of representative nodes:

$$\frac{dV_i}{dt} = f(V_i) + \sum_j^N w_{ij}\delta_{ij}g_{ij}(V_i), \quad (8)$$

where $f(V_i)$ is a function of the membrane potential V_i , representing the individual dynamics of each neuron, and the second term is from Eq. (4), corresponding to the synaptic current between the motifs. The discrete form of Eq. (8) is obtained by employing the Euler method:

$$V_i^{t+\Delta t} = V_i^t + f(V_i^t)\Delta t + \sum_j^N w_{ij}\delta_{ij}g_{ij}(V_i^t)\Delta t, \quad (9)$$

where Δt is the time step in numerical simulation. Next, in addition to the connectivity weight w_{ij} , Eq. (10) is categorized as follows:

$$\begin{aligned} x_{i_0}^t &= V_i^t + f(V_i^t)\Delta t, \\ x_{i_1}^t &= \delta_{i_1}g_{i_1}(V_i^t)\Delta t, \\ &\vdots \\ x_{i_n}^t &= \delta_{i_n}g_{i_n}(V_i^t)\Delta t. \end{aligned} \quad (10)$$

Express the aforementioned system of equations in matrix form: $x_i^t = [x_{i_1}^t, x_{i_2}^t, \dots, x_{i_n}^t]^T$, and weight w_{ij} could be represented by the similar way: $w_i^t = [w_{i_1}^t, w_{i_2}^t, \dots, w_{i_n}^t]^T$. Then Eq. (9) can be rewritten as:

$$V_i^{t+\Delta t} = x_{i_0}^t + w_i^T \times x_i^t. \quad (11)$$

In the self-adaptive DLS technique utilized in this research, the contrast value $\bar{V}_{t+\Delta t}$ is ascertained by calculating the mean membrane potential of all nodes within the network that are subject to weight modifications throughout the learning process [29].

$$\bar{V}_{t+\Delta t} = \frac{1}{N} \sum_i^N V_i^{t+\Delta t}. \quad (12)$$

Incorporating Eq. (10), the collective set of these values across all time steps is represented in matrix notation as:

$$\begin{aligned} \bar{V} &= [\bar{V}_{t_2}, \bar{V}_{t_3}, \dots, \bar{V}_{t_{m+1}}]^T, \\ X_i^{m \times n} &= [x_{i_1}^{t_1}, x_{i_1}^{t_2}, \dots, x_{i_1}^{t_m}]^T, \\ X_{i_0} &= [x_{i_0}^{t_1}, x_{i_0}^{t_2}, \dots, x_{i_0}^{t_m}]^T. \end{aligned} \quad (13)$$

The objective in achieving synchronization of the i th node with other nodes in the network is to minimize the squared difference between the node's value at the subsequent time step, as predicted by Eq. (8), and a reference value. This minimization process of the error can be expressed as:

$$E = \arg \min \frac{1}{2} \sum_{t=t_1}^{t_m} (w_i^T \times x_i^t + x_{i_0}^t - \bar{V}_{t_{m+1}})^2. \quad (14)$$

Then, combining the average contrast value $\bar{V}_{t+\Delta t}$ and $x_{i_0}^t$ time series of Y_i could be shown in matrix form as follows:

$$Y_i = \bar{V}_{t+\Delta t} - x_{i_0}^t \\ = [\bar{V}_{t_2} - x_{i_0}^{t_1}, \bar{V}_{t_3} - x_{i_0}^{t_2}, \dots, \bar{V}_{t_{m+1}} - x_{i_0}^{t_m}]^T. \quad (15)$$

Equation (14) could be rewritten as:

$$E = \arg \min \frac{1}{2} (X_i w_i - Y_i)^T (X_i w_i - Y_i). \quad (16)$$

Then, the gradient of the error (E) with respect to the weights (w_i) is denoted as follows:

$$\frac{dE}{dw} = X_i^T (X_i w_i - Y_i). \quad (17)$$

As the error originates from the square of the difference, according to the principles of the least-square method, the optimal value is determined by minimizing the square of this error. The optimal weight values are computed as:

$$w_i = (X_i^T X_i)^{-1} X_i^T Y_i. \quad (18)$$

The subsequent step involves determining the optimal weights w_i predicated on the time series data of X_i and Y_i . The intricacies of the derivation are elaborated in our previous work [29], with the recursive formula for these optimal weights given by:

$$w_i^{t_{m+1}} = w_i^{t_m} - k_i^{t_m} \left((x_i^{t_{m+1}})^T w_i - Y_i^{t_{m+1}} \right), \\ k_i^{t_m} = \frac{P_i^{t_m} x_i^{t_{m+1}}}{1 + (x_i^{t_{m+1}})^T P_i^{t_m} x_i^{t_{m+1}}}, \\ P_i^{t_{m+1}} = \left(I - k_i^{t_m} (x_i^{t_{m+1}})^T \right) P_i^{t_m}, \quad (19)$$

where k_i denotes the learning rate of w_i . According to Eq. (19), we can dynamically update weights using the DLS technique until the error value reaches a minimum, and the network attains a stable state. In this algorithm formula, $x_i^{t_{m+1}} = [x_{i_1}^{t_{m+1}}, x_{i_2}^{t_{m+1}}, \dots, x_{i_n}^{t_{m+1}}]^T$ are coupled data generated within a nonlinear system. $w_i = [w_{i_1}, w_{i_2}, \dots, w_{i_n}]^T$ represent the connection weights between the i th node and other nodes requiring weight regulation in the nonlinear system. The variable $Y_i^{t_{m+1}}$ is designated as shown in Eq. (15).

The fundamental principle of the DLS technique revolves around the continuous update of learnable parameters within a coupled system. This update process utilizes values produced by a nonlinear oscillator and their corresponding reference values, establishing a recursive connection with preceding values. Owing to the recursive characteristic of the parameter updating mechanism, an initial value must be set at the beginning of the iteration process. According to Eq. (19), the initial value for the iterative variable P_i is typically chosen

as: $P_i^{t_0} = \alpha I$, in which I is the identity matrix and α is a hyperparameter. In this study, α is set to 0.01 unless specified otherwise.

Within the framework of the DLS technique, as outlined by Eqs. (9) and (15), the dynamic representation of the nonlinear system described in Eq. (1) is reformulated as follows to facilitate weight modulation:

$$X_i^{t_{m+1}} = [\delta_{i_1} g_{i_1} (V_i^{t_{m+1}}) \Delta t, \dots, \delta_{i_N} g_{i_N} (V_i^{t_{m+1}}) \Delta t]^T, \\ Y_i^{t_{m+1}} = \frac{1}{n} \sum_i V_i^{t_{m+1}} \\ - [V_i^{t_m} + (-I_{Na} - I_K - I_L + I_{ext} + I_{syn_1}) \Delta t / C_m]. \quad (20)$$

During numerical simulation, the objective of synchronizing the complex system is accomplished by iteratively adjusting the weights w_i while continuously iterating over $X_i^{t_{m+1}}$ and $Y_i^{t_{m+1}}$.

C. Quantitative synchronization

Investigations into network synchronization highlight the importance of quantifying synchronization levels within the network for effective visualization. The principal measure used for this purpose is the standard deviation (e) of membrane potentials across all nodes, with a lower e signifying greater synchronization among neurons. This study is particularly concentrated on applying the DLS technique to modulate network weights, thereby aiming to improve network synchrony. The effectiveness of this weight modulation is monitored through the variation of e over time. The mathematical expression for the standard deviation of membrane potentials is provided below:

$$e = \sqrt{\frac{1}{N} \sum_{i=1}^N \left(V_i - \frac{1}{N} \sum_{i=1}^N V_i \right)^2}. \quad (21)$$

Although the standard deviation of membrane potentials across all nodes offers an initial gauge of synchronization—where a smaller standard deviation implies better synchronization—it falls short in accuracy and detail for comprehensive analysis. To standardize the observation of network synchronization more effectively, this study introduces a concept from statistical physics known as the synchronization factor R . Its mathematical expressed as:

$$R = \frac{\langle F^2 \rangle - \langle F \rangle^2}{\frac{1}{N} \sum_{i=1}^N (\langle V_i^2 \rangle - \langle V_i \rangle^2)}, \quad F = \frac{1}{N} \sum_{i=1}^N V_i. \quad (22)$$

The computation of this factor accurately mirrors the spatiotemporal synchronization state of neurons within the network. By analyzing the synchronization factor under diverse conditions, an intuitive examination of the levels of synchronization and the transitions therein across the network is facilitated. In Eq. (8), V_i represents the membrane potential as determined by Eq. (1). N denotes the total number of motifs in the complex network. The symbol $\langle * \rangle$ represents the average value of the variable throughout the computation process. A synchronization factor R nearing 1 signifies a higher degree

of synchronization, implying that the nodes are more closely aligned in their activities. On the other hand, an R value approaching 0 indicates poorer synchronization, indicating a disparity in the nodes' consistency. As a standardized statistical metric, the synchronization factor accurately measures the extent of synchronization among nodes within the network.

III. RESULTS

In this section, we delve into the effects of dynamic learning of synchronization (DLS) techniques on adjusting weights to enhance the synchronicity of the higher-order motif network. The discussion also encompasses the intrinsic mechanisms of external stimulation changes during the adjustment process, providing an in-depth exploration of these complex dynamic processes. This study employs the Euler forward algorithm to numerically solve the nonlinear dynamic equations represented by Eqs. (1) and (8). When computing Eq. (1), the integration step size Δt is set to 0.01. Additionally, the constant external stimulation I_{ext} for each node is determined by Gaussian distributed values with a mean of $10 \mu\text{A}/\text{cm}^2$ and a standard deviation of 1.

A. Modulation by the DLS techniques among specific neurons in the higher-order motif network

Initially, we examine a scenario in the higher-order motif network where only individual nodes between each motif are connected, utilizing the DLS technique to fine tune the connection weights and investigating whether the network can reach a state of synchronization after adjustment. For the sake of clarity, all motifs are interconnected exclusively through neuron 3, which is appointed as the output terminal, to assess the efficacy of synchronization following the application of the DLS technique. The initial connection weights between output neurons are assigned randomly, with electrical synapses weights ranging from -0.02 to 0.02 .

Figure 2 illustrates the results of analyzing an ER random graph structure with motifs interconnected by electrical synaptic coupling. This setup is used to assess the effect of the DLS technique. The ER random graph network is structured with an average node degree in about 6. The simulation is segmented into distinct phases: (i) initialization; (ii) training; (iii) testing; succeeded by (iv) an attack phase—during which, connections bearing weights exceeding 6 are disconnected to provoke a loss of synchronization; (v) retraining; (vi) retesting. These stages are repeatedly conducted 20 times, and the average standard deviation of the membrane potentials obtained from each simulation is presented in Fig. 2(a). The firing raster diagram of the output neurons are plotted by Figs. 2(b) and 2(c). To examine the firing dynamics of individual neurons, Figs. 2(d) and 2(e) depict the time series of membrane potentials of the output neurons corresponding to the 20th and the 80th motif, respectively.

During the initialization phase, the standard deviation e of the average membrane potential of the output neurons across 20 simulations is within a relatively high range, indicating a disordered firing state and nonsynchronous activity among the output neurons. Upon the introduction of the DLS technique at moment T1 to modulate the connection weights

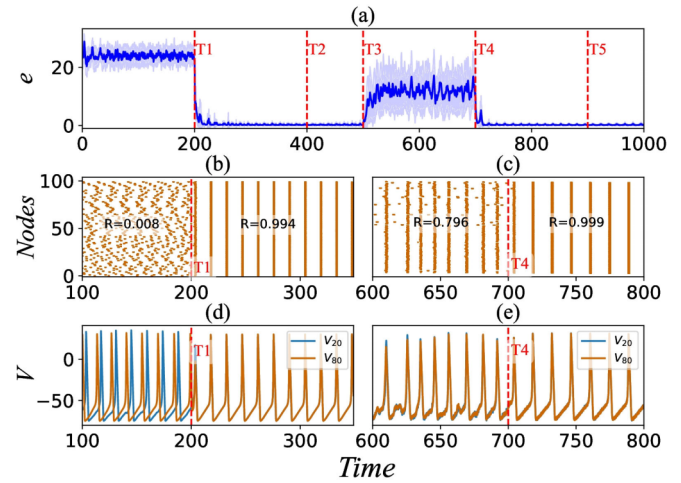


FIG. 2. The efficacy of the DLS technique in the ER random graph motif network with a connection probability of $p = 0.06$ is examined. The experimental process is divided into six phases: (i) initialization; (ii) training; (iii) testing; (iv) attack connections with weights exceeding 6 are disconnected to induce desynchronization; (v) retraining; (vi) retesting. Key time points T1, T2, T3, T4, and T5 are set at 200 ms, 400 ms, 500 ms, 700 ms, and 900 ms, respectively. The simulation is repeated 20 times, and the standard deviation of the membrane potentials from each simulation is averaged to produce (a). (b) and (c) depict the firing raster during different phases from one of the repetitions. (d) and (e) display the time series of the membrane potentials for the output neurons corresponding to the 20th and the 80th motif in the network during various phases.

between output neurons, there is a noticeable reduction in e to a lower value, indicating enhanced synchronization. This improved state of synchronization is evident from the spike raster Fig. 2(b) and the time series of the output neurons' membrane potentials Fig. 2(d), where the synchronization factor R reaches 0.994 during the training phase, signifying a transition from a disordered to a synchronized state among the output neurons.

After the training phase, testing of the network's firing state was conducted at moment T2. Following adjustments to the connection weights, the standard deviation of the average membrane potential e remained consistently low, indicating a stable synchronization. This stable firing state of the output neurons is observable from Fig. 2(b) the firing raster and 2(d) the time series of membrane potential.

To test the stability of the synchronization training effect of the DLS technique, an attack test was conducted on the network. To compromise for the network's synchrony, connections with weight values $w > 6$ were disconnected, which accounted for approximately 5% of all weight values. Additionally, Gaussian white noise with an intensity $D = 20$ was introduced. It was observed that the network's synchrony was somewhat disrupted, and e of the average membrane potential resumed its ascent to relatively high values during this phase. The impact of disconnecting a certain number of weights and noise on the synchronized state can be seen from Figs. 2(c) and 2(e). Notably, the synchronization factor R declines to 0.796, indicating a reduction in synchrony. Subsequently, the network was trained again after moment T4, with the same

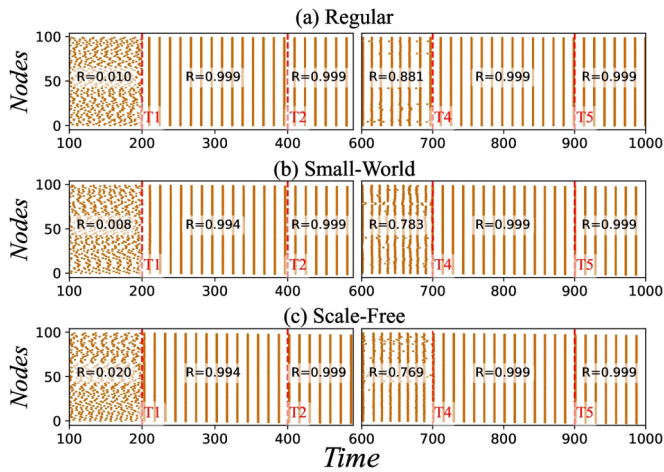


FIG. 3. Firing raster diagrams for the other three networks under the implementation of the DLS technique, with experimental phases consistent with Fig. 2. The firing raster of (a) regular motif network, (b) small-world motif network, (c) scale-free motif network. All three networks showed good effects in achieving a synchronized state after the initial training and again after being subjected to an attack and retrained.

intensity of noise applied as during the attack phase, to observe the training effect of the DLS technique under the influence of noise. Figures 2(c) and 2(e) show that the network rapidly regained a synchronized state following DLS training. This demonstrates that DLS significantly improves the adaptability of higher-order motif networks against connectivity adjustments and external disruptions, allowing them to efficiently achieve regular firing states even amid changes in the external environment. Furthermore, the time series of membrane potential in Fig. 2(e) demonstrates that even in the presence of noise disturbances, the DLS technique can still adjust the connection weights between motifs, achieving a regular firing state.

Next, firing raster for three other types of networks are drawn to observe the modulatory effects of the DLS technique within these networks. Figure 3(a) displays the scenario simulated in a regular network. Consistent with the ER random graph network, the output neurons of the higher-order motif network can achieve a synchronized state after the initial training, with the synchronization factor R reaching 0.999. During the attack phase, connections with weight values $w > 0.3$ are disconnected, and the impact of noise on neurons is considered. The basic principle behind selecting different thresholds for disconnection: We aimed to induce desynchronization in the attacked networks by disconnecting connections with larger weights. In biological neural networks, larger-weight synapses often correspond to critical information pathways. Besides, for comparison with Fig. 2, we chose thresholds that ensure similar levels of desynchronization across the network types (excluding the regular network), allowing for a more meaningful comparative analysis under comparable conditions. The regular network maintains better synchronization even when a similar or greater proportion of connections are disrupted compared to other heterogeneous networks. The synchronization factor R can still reach 0.881, indicating a relatively synchronized state. This is attributed to the regular

distribution of connections among nodes in the regular network, where disconnecting some connections has a smaller impact on the network's firing state compared to other nonuniform networks. Similarly, after further training, the network once again achieves a synchronized state.

The simulation scenario for the small-world network is depicted in Fig. 3(b). The small-world network used in this experiment has a connection probability of 0.06 and a rewiring probability of 0.5. The process and results of the initial training are similar to those of the two networks mentioned earlier, showing that the DLS technique also effectively modulates the small-world motif network. The attack on this network is by disconnecting connections in the well-trained network with weight values $w > 4$, along with the introduction of Gaussian white noise. During the attack phase, the synchrony of the small-world network is significantly impaired, with the synchronization factor R decreasing to 0.783. However, after retraining, a good synchronized state is once again achieved, and synchronization factor R is increased to 0.999.

For the case of scale-free motif network shown in Fig. 3(c), the initial state of the network consists of seven interlinked motifs. Subsequently, each new motif added connects to three old motifs. This setting ensures a connection probability of about 0.06, consistent with the other two types of irregular motif networks. Similar to the other three networks, modulation of the weights between output neurons using the DLS technique allows the transition of the output neurons' firing condition from a disordered to a synchronized state. The attack on the scale-free network is manifested by disconnecting connections with weight values $w > 8$ in the well-trained network and incorporating the effect of Gaussian white noise, resulting in the synchronization factor R dropping to 0.769. After further training of the network, the firing state among output neurons is restored to synchrony. It can be observed that when motifs are interconnected through electrical synapses, the DLS technique demonstrates effective training outcomes across all four types of higher-order motif networks.

Following our previous analysis, we are now acquainted with the effects of the DLS technique across four types of higher-order motif networks. Next, we will examine the distribution of the connection weights among output neurons after modulation by the DLS technique within these networks. Figure 4 displays the weight histograms for each network after adjustment, with the initial weight distributions shown as insets in the top right corner of each panel. In each higher-order motif network, the initial values of the connection weights for the output neurons are uniformly distributed. It can be observed that after the implementation of the DLS technique, the weight distributions in all networks have transitioned to a Gaussian-like case. In this scenario, the distribution of weights is predominantly centered around the region close to 0, with the number of weights on either side gradually decreasing. For the regular motif network, as shown in Fig. 4(a), the connection weights between output neurons are generally lower than in the other three network structures. This is primarily because each node in the regular network has more connections, equating to a greater number of weights available for adjustment, thereby requiring smaller weight values to achieve a synchronized state.

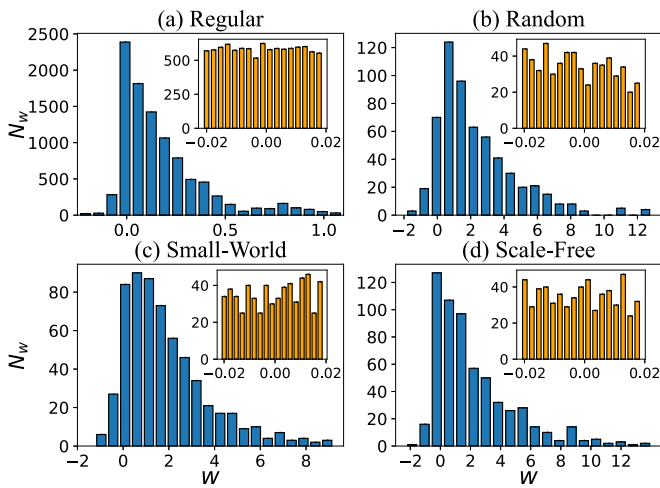


FIG. 4. The histograms showing the distribution of weights after training in each motif network as depicted: (a) regular motif network, (b) ER random graph motif network, (c) small-world motif network, and (d) scale-free motif network. The initial weight distributions are shown as insets in the top right corner of each panel. Following the implementation of the DLS technique, the weight distributions for the four motif networks exhibit a central peak within the lower range of w . On both sides of this central peak, the number of weights N_w gradually decreases, resulting in a right-skewed distribution.

Apart from the regular network, the other three heterogeneous networks have an average degree set to around 6. Among the three irregular networks, the small-world network, as shown in Fig. 4(c), has the smallest range of weight distribution. Additionally, the quantity of weights predominantly clustered around the center of the distribution is also lower than that in the other two irregular network. However, the characteristic that most weight values are close to 0 is consistent with other network structures. The scale-free motif network exhibits the highest degree of dispersion among the irregular network structures, as illustrated in Fig. 4(d). The proportion of negative weights is also higher in the scale-free network than in the other networks, possibly because a few nodes in the scale-free network are connected to a large number of nodes, requiring more negative weights to achieve a balanced state. Moreover, the number of weights near the central peak is significantly higher in random and scale-free networks compared to the small-world network.

Given that regular networks more readily achieve synchronization under the same conditions, the focus of the subsequent discussion regarding weight distribution will primarily rest on the three heterogeneous networks. To further analyze the pattern of weight changes during the network synchronization process facilitated by the DLS technique, we illustrate the time evolution of the weight distribution between output neurons in the three types of irregular networks on the left column of Fig. 5, with different colors representing the number of weights in the network. Curves representing the average weight as a function of time are also added to the left column of panels. These curves show that the initial weights are randomly distributed around a small value before training. As training progresses, the average weight increases and eventually stabilizes at a higher value, indicating the

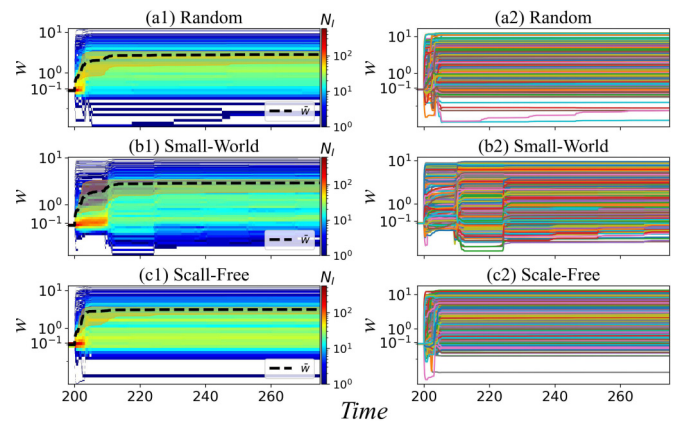


FIG. 5. Changes in weights over time during the training process in three types of irregular higher-order motif networks. The left column presents time series histograms of weights, showing the distribution of weights at each moment under the influence of the DLS technique. The dashed line shows the average weight over time with shading to convey the standard deviation from multiple tests. The right column depicts the changes in the value of each connection weight over time during the DLS technique’s application. (a) The ER random graph motif network. (b) The small-world motif network. (c) The scale-free motif network.

emergence of larger weights that regulate the collective behavior of neurons. Additionally, summary line graphs depicting the temporal evolution of each connection weight are presented on the right column of Fig. 5. It can be observed that the connection weights in all three networks undergo a transition from an initially concentrated distribution to a broader distribution. Compared to the other two network structures, the small-world network requires more time to evolve to a final stable state. The weights reached a relatively stable distribution in a short period of time, indicating that DLS technique not only enhances the adaptability of higher-order network synchronization but also improves the efficiency of the synchronization process.

Furthermore, as seen from Fig. 5(b1), the overall color of the heat map is lighter, indicating a more uniform distribution of weight values, which corroborates the results obtained from the histogram shown in Fig. 4(c). The emergence of such a weight distribution could be attributed to the small-world network’s characteristics of having shorter average path lengths and a high number of local connections. These features likely lead to a slightly narrower range of weight values in the network’s weight distribution upon achieving synchronization. In contrast, the scale-free network exhibits a larger proportion of smaller weights, with only a few connections having significantly larger weight values. In Fig. 5(c1), it can be observed that the area representing smaller weight values is brighter, indicating a larger proportion of these weights in the scale-free network. Only a few connections have significantly larger weight values. This may be attributed to the heterogeneity of the scale-free network, where a minority of nodes accumulate a large number of connections. These few nodes significantly impact the overall dynamical characteristics of the network [41].

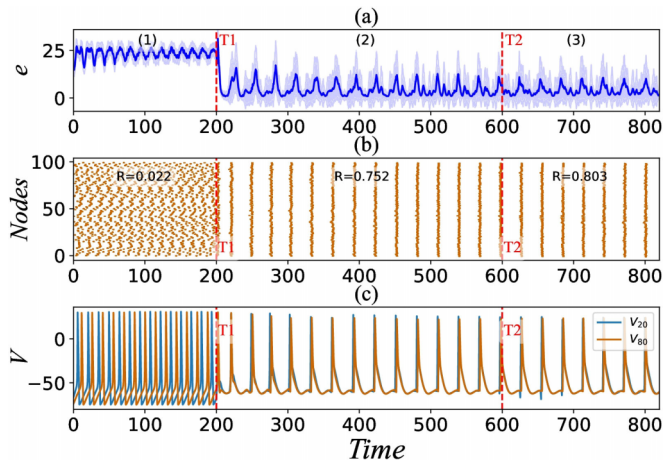


FIG. 6. The efficacy of the DLS technique in ER random graph motif networks connected by chemical synapses with a connection probability of $p = 0.06$ is examined. The experiment is divided into three stages: (i) initialization; (ii) training; (iii) testing. Key moments T1 and T2 are set at 200 ms and 600 ms, respectively. The simulation is repeated 20 times. (a) Averages the standard deviation of membrane potentials across 20 simulations. (b) Firing raster diagram from a single simulation through different phases. (c) Time series of membrane potentials in the output neurons of the 20th and 80th motifs.

Following the discussion above, we have learned that the DLS technique has a good effect on synchronizing higher-order motif networks connected by electrical synapses. Next, we will analyze the effect of this technique on the regularization of firing patterns of output neurons within higher-order motif networks, which are connected by chemical synapses. The initial connection weights between output neurons are randomly assigned, ranging from 0–0.02. We will also start with the ER random graph as an example, and the entire simulation process is divided into the following stages: (i) initialization, (ii) training, (iii) testing. To achieve better synchronization with chemical synapses, a longer training period is required than electrical synapses. The training duration was determined through testing to achieve a stable firing state. Since the training effectiveness of chemical synapses is weaker compared to electrical synapses, a longer duration of 400 ms was set to achieve stability. The simulation process is repeated 20 times, and the standard deviation of the membrane potentials from each simulation is averaged to produce Fig. 6(a), with the firing raster of the output neurons illustrated in Fig. 6(b). Similarly, Fig. 6(c) displays the time series of the membrane potentials for the output neurons of the 20th and 80th motifs.

In Fig. 6(a), it can be observed that before the adjustment of weights using the DLS technique, the firing state among output neurons was disordered, and the standard deviation of the membrane potentials was relatively high. After the implementation of the DLS technique at moment T1, the standard deviation of the membrane potentials rapidly decreased. In conjunction with the raster in Fig. 6(b), it can be seen that the output neurons gradually achieved a synchronized firing state. Although there are numerical fluctuations, e decreases again at the moments of spiking. Unlike the more

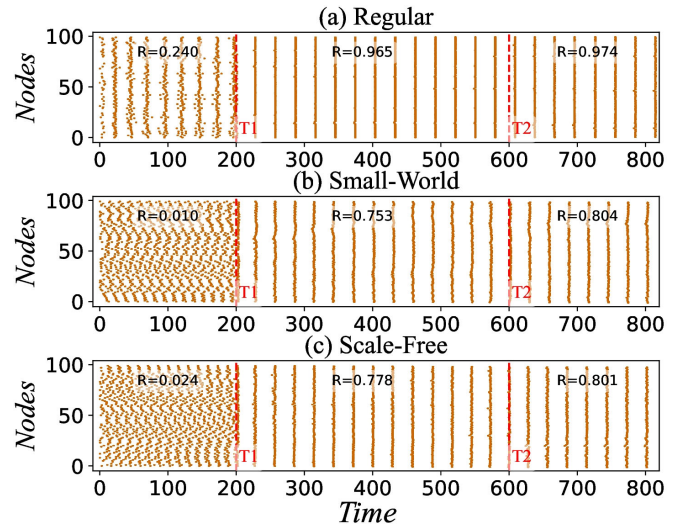


FIG. 7. Firing raster diagrams of output neurons in three other motif higher-order networks connected by chemical synapses. The experimental process is consistent with that depicted in Fig. 6. (a) Regular motif network, (b) small-world motif network, (c) scale-free motif network. These three networks all exhibit good synchronization states after training with the DLS technique.

synchronized firing state of higher-order motif networks connected by electrical synapses, those trained with the DLS technique for chemical synapses still exhibit some degree of disorder. This is also reflected in the synchronization factor R , which was 0.803 during the testing phase for the random motif network with chemical synapses, indicating a lesser synchronization effect compared to the electrical synapse scenario. This may be because electrical synapses, as part of a diffusion system have a stronger synchronization capability and can achieve a better synchronized state more rapidly. Figure 6(c) displays the time series of the membrane potentials, showing that the firing rate before the application of the DLS technique was higher than after. This may be because, to achieve a dynamic equilibrium state, the neurons reduce their dynamic response frequency, allowing synchronized activity to persist at a lower firing rate. Thus, in higher-order motif networks connected by chemical synapses, synchronization among output neurons can also be achieved through the application of the DLS technique.

Similarly, we have depicted the firing raster for three types of higher-order motif networks connected by chemical synapses, as shown in Fig. 7. Due to the chemical synapses' significant impact only at the moment of neuronal firing, analyzing the synchronization of chemical synaptic systems is more complex. As Fig. 7 shows, it can be observed that the synchronization effect in the regular network remains the best among the networks. After the DLS technique has adjusted the weights, the synchronization factor R between output neurons can reach 0.974, indicating a good state of synchronization. For the small-world and scale-free networks, the synchronization factors R after DLS training are 0.804 and 0.801, respectively, which represent a synchronized state compared to the disordered state before training. This demonstrates that

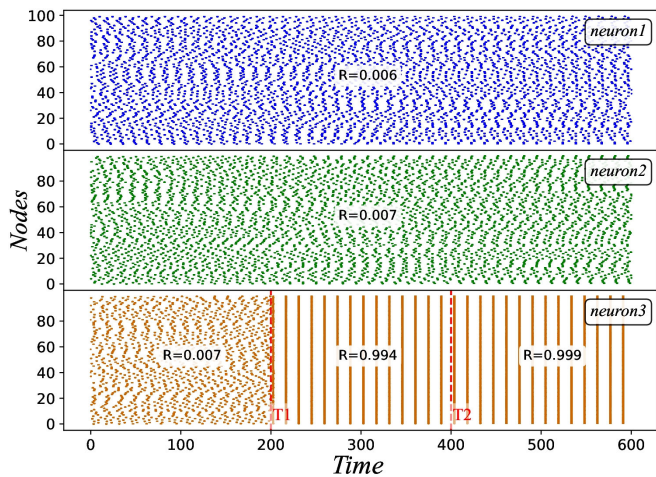


FIG. 8. The firing raster diagrams for all neurons in the network when connections between motifs are electrical synapses, and the DLS technique is applied only to specific neuronal connections. During the testing phase, the synchronization factor between output neurons is $R = 0.999$, with only node 3 achieving a synchronized state.

the DLS technique still effectively regulates regular neuronal spikes in the other three networks. However, both in terms of the time required to adjust weights and the effect of synchronization achieved, the synchronization effect between output neurons connected by chemical synapses is inferior to those connected by electrical synapses.

B. Modulation by the DLS techniques among multiple neurons in the higher-order motif network

In previous sections, we analyzed the simplest motif networks where only output neurons are connected, focusing solely on the firing patterns of these output neurons without considering the firing states of the other two neurons. Next, we will address a more realistic scenario where the output neuron can connect with all neurons within the network, and we will illustrate the firing patterns of all neurons in the network. As shown in Fig. 8, taking a random motif network as an example, in the higher-order motif networks connected by electrical synapses, the connections between output neurons, after being trained with the DLS technique, show that only the output neurons have achieved a synchronized firing state, with the post-training synchronization factor R reaching 0.999. The firing states of neuron 1 and neuron 2, which were not adjusted by the DLS technique, remain disordered.

Similarly, this phenomenon can be observed in higher-order motif networks connected by chemical synapses. As shown in Fig. 9, when the DLS technique is applied only to the connections between output neurons, only the firing state of the output neurons achieves synchronization, with the post-training synchronization factor R reaching 0.803. The firing states of the other two neurons remain disordered. We aim to analyze the regulatory effect of the DLS technique on the entire higher-order motif network. Next, we will apply the DLS technique to all connections between motifs, i.e., adjusting the connection weights between the output

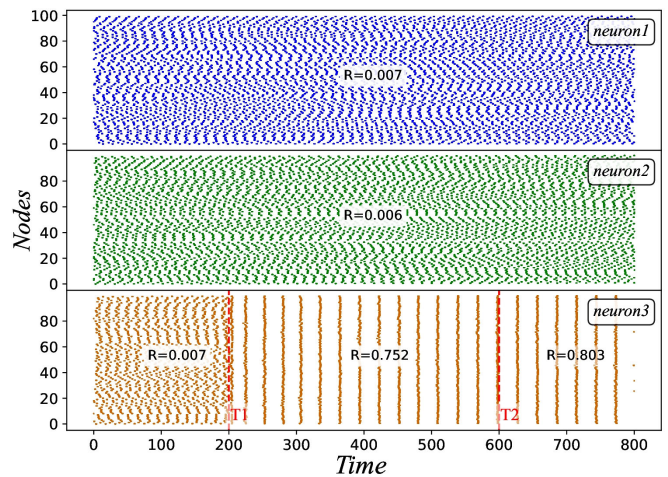


FIG. 9. The firing raster diagrams for all neurons in the network when connections between motifs are chemical synapses, and the DLS technique is applied only to specific neuronal connections. During the testing phase, the synchronization factor between output neurons is $R = 0.803$, with only node 3 achieving a synchronized state.

neuron and other nodes within the entire higher-order motif network, and then observe the synchronization of the entire network.

In Fig. 10, it can be seen that when the DLS technique is applied to modulate the connection weights between motifs, all neurons in the network can achieve a synchronized state. Consistent with the synchronization effect of training between individual neurons, when the DLS technique adjusts the connection weights between all motifs, the electrical activity of all neurons in the network reaches a synchronized state. Therefore, we can suggest that the DLS technique has a good training effect in the higher-order motif networks connected by electrical synapses.

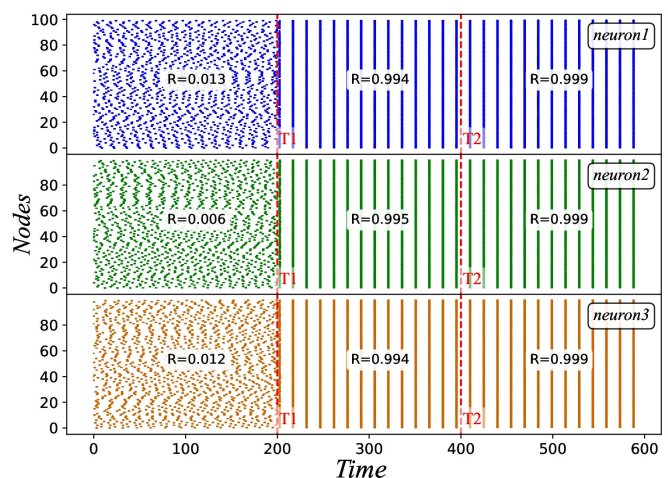


FIG. 10. The firing raster diagrams for all neurons within the network, when motifs are interconnected via electrical synapses and the DLS technique is applied to adjust the weights of all connections between motifs. Nodes 1, 2, and 3 all achieve a synchronized state during the testing phase, with the entire network's firing state reaching synchronization.

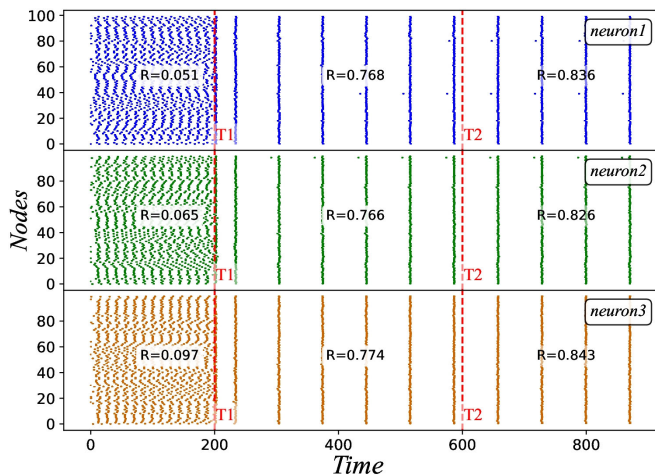


FIG. 11. The firing raster diagrams for all neurons within the network, when motifs are interconnected via chemical synapses and the DLS technique is applied to adjust the weights of all connections between motifs. Nodes 1, 2, and 3 all achieve a synchronized state during the testing phase, significantly enhancing the overall network's synchronicity.

In the higher-order motif network connected by chemical synapses, the firing raster Fig. 11 reveals that all neurons achieve a synchronized state after modulation with the DLS technique. Following the adjustment of weights by the DLS technique, the synchronization factors R for neurons 1, 2, and 3 are 0.836, 0.826, and 0.843. To compare the synchronization levels of neurons 1, 2, and 3, we repeated the simulation process more than 20 times and calculated the mean and standard deviation of the synchronization factors obtained from these simulations. The mean synchronization factors (\pm standard deviation) are $\bar{R}_1 = 0.8146 \pm 0.0266$, $\bar{R}_2 = 0.8197 \pm 0.0217$, and $\bar{R}_3 = 0.8254 \pm 0.0193$. The small differences in the mean synchronization factors indicate that the synchronization states of neurons 1, 2, and 3 are essentially identical. With the same initial parameters and compared to the scenario where only the weights between output neurons are adjusted, the synchronicity among all nodes is enhanced, and every node in the network reaches a state of synchronization, leading to an overall synchronized state in the higher-order motif network. However, the overall firing rate of the network significantly decreases, which may be because, in order to achieve a dynamic equilibrium state, each neuron reduces its dynamic response frequency, allowing synchronized activity to persist at a lower firing rate. The number of neurons achieving synchronization in the entire motif network is much greater than when only the output neurons are synchronized, leading to a reduction in the firing rate of network nodes as a result.

From the analysis above, whether the higher-order motif networks are connected by electrical or chemical synapses, when the DLS technique is applied to modulate the connection weights among all motifs, the network can achieve an overall synchronized state. This indicates that the DLS technique has a good regulatory effect on the spike rhythm of the motif network.

IV. CONCLUSIONS

This investigation thoroughly examines the utilization and efficacy of the dynamic learning of synchronization (DLS) technique for promoting synchronicity within high-order networks. We analyzed the impact of the DLS technique on the dynamics of the higher-order motif networks, which are composed of triplet motifs, each consisting of three Hodgkin-Huxley neurons. Various combinations of motifs were considered, including topological structures such as regular, ER random graphs, small-world, and scale-free networks. The DLS technique enhances network synchronicity by adjusting the weights between relevant nodes within the network.

Results indicate that when only the connection weights between output neurons of motifs are modulated by the DLS technique, the firing state between output neurons transitions from disorder to order after training. Furthermore, in the various analyzed higher-order motif network structures, the firing state between output neurons can be synchronized. Taking electrical synapses as an example and analyzing the changes in connection weights throughout the adjustment process, it was found that the connection weights transition from an initial uniform random distribution within a small range to a more dispersed distribution. Different higher-order motif network structures exhibit distinct weight distribution states after adjustment by the DLS technique, the evolution of weight correlates with the network's topological structure. For motifs interconnected via chemical synapses, the DLS technique can still synchronize the output neurons, but the synchronization effect is slightly inferior to that in the case of electrical synapses, and the firing rate of the output neurons declines.

Finally, taking the random motif network as an example, we analyzed a more realistic scenario where output neurons can connect with all neurons within the network. It was found that when the DLS technique is applied to all connection weights between motifs, all nodes can achieve a synchronized state, regardless of whether the connections between motifs are electrical or chemical synapses. However, the overall degree of synchronization in higher-order motif networks connected by chemical synapses remains weaker than that in networks with electrical synapses. In summary, DLS offers a highly adaptive synchronization strategy to network changes and external disturbances. It can facilitate the emergence of synchronized states in highly complex nonlinear networks. Based on this study, future work will focus on the application of DLS technology in more practical systems and models, attempting to provide a deeper understanding of synchronization issues from a more realistic perspective.

ACKNOWLEDGMENTS

This work is supported by National Natural Science Foundation of China under Grant No. 12175080, and also financially supported by self-determined research funds of CCNU from the colleges' basic research and operation of MOE under No. CCNU22JC009.

- [1] J. F. Mejías and X. J. Wang, Mechanisms of distributed working memory in a large-scale network of macaque neocortex, *eLife* **11**, e72136 (2022).
- [2] R. Borisyyuk, A. Khibnik, A. N. Balachandar, and J. Tabak, From phase advance to phase delay: Flexible coordination between neuronal rhythms by the duration of synaptic input, *Phys. Rev. Res.* **5**, 033017 (2023).
- [3] A. Uchida, R. McAllister, and R. Roy, Consistency of nonlinear system response to complex drive signals, *Phys. Rev. Lett.* **93**, 244102 (2004).
- [4] R. C. Budzinski, K. L. Rossi, B. R. R. Boaretto, T. L. Prado, and S. R. Lopes, Synchronization malleability in neural networks under a distance-dependent coupling, *Phys. Rev. Res.* **2**, 043309 (2020).
- [5] D. Yu, L. Lu, G. Wang, L. Yang, and Y. Jia, Synchronization mode transition induced by bounded noise in multiple time-delays coupled FitzHugh–Nagumo model, *Chaos, Solitons Fractals* **147**, 111000 (2021).
- [6] A. Buehlmann and G. Deco, Optimal information transfer in the cortex through synchronization, *PLOS Comput. Biol.* **6**, e1000934 (2010).
- [7] L. Lu, M. Ge, Y. Xu, and Y. Jia, Phase synchronization and mode transition induced by multiple time delays and noises in coupled FitzHugh–Nagumo model, *Physica A* **535**, 122419 (2019).
- [8] T. Li, G. Wang, D. Yu, Q. Ding, and Y. Jia, Synchronization mode transitions induced by chaos in modified Morris–Lecar neural systems with weak coupling, *Nonlinear Dyn.* **108**, 2611 (2022).
- [9] R. Milo, S. Shen-Orr, S. Itzkovitz, N. Kashtan, D. Chklovskii, and U. Alon, Network motifs: Simple building blocks of complex networks, *Science* **298**, 824 (2002).
- [10] X. Liang, S. Yanchuk, and L. Zhao, Gating-signal propagation by a feed-forward neural motif, *Phys. Rev. E* **88**, 012910 (2013).
- [11] F. Mori and T. Okada, Information-transfer characteristics in network motifs, *Phys. Rev. Res.* **5**, 013037 (2023).
- [12] Z. Ye, Y. Yang, and Y. Jia, Inverse stochastic resonance in Izhikevich neural motifs driven by Gaussian colored noise under electromagnetic induction, *Int. J. Mod. Phys. B* **37**, 2350049 (2023).
- [13] A. R. Benson, D. F. Gleich, and J. Leskovec, Higher-order organization of complex networks, *Science* **353**, 163 (2016).
- [14] F. Battiston, E. Amico, A. Barrat, G. Bianconi, G. F. de Arruda, B. Franceschiello, I. Iacopini, S. Kéfi, V. Latora, Y. Moreno, M. M. Murray, T. P. Peixoto, F. Vaccarino, and G. Petri, The physics of higher-order interactions in complex systems, *Nature Phys.* **17**, 1093 (2021).
- [15] S. Majhi, M. Perc, and D. Ghosh, Dynamics on higher-order networks: a review, *J. R. Soc. Interface* **19**, 20220043 (2022).
- [16] A. Olamat, P. Ozel, and A. Akan, Synchronization analysis in epileptic EEG signals via state transfer networks based on visibility graph technique, *Int. J. Neur. Syst.* **32**, 2150041 (2022).
- [17] A. Galvan and T. Wichmann, Pathophysiology of parkinsonism, *Clin. Neurophysiol.* **119**, 1459 (2008).
- [18] S. Abadal and I. F. Akyildiz, Bio-inspired synchronization for nanocommunication networks, in *2011 IEEE Global Telecommunications Conference - GLOBECOM 2011* (IEEE, Houston, 2011), pp. 1-5.
- [19] A. Ascoli, R. Tetzlaff, V. Lanza, and F. Corinto, Synchronization properties of a bio-inspired neural network, in *2015 IEEE 15th International Conference on Nanotechnology* (IEEE, Rome, 2015), pp. 621-624.
- [20] S. Song, P. J. Sjöström, M. Reigl, S. Nelson, and D. B. Chklovskii, Highly nonrandom features of synaptic connectivity in local cortical circuits, *PLOS Biol.* **3**, e68 (2005).
- [21] Q. F. Lotito, F. Musciotto, A. Montresor, and F. Battiston, Higher-order motif analysis in hypergraphs, *Commun. Phys.* **5**, 79 (2022).
- [22] J. T. Lizier, F. Bauer, F. M. Atay, and J. Jost, Analytic relationship of relative synchronizability to network structure and motifs, *Proc. Natl. Acad. Sci.* **120**, e2303332120 (2023).
- [23] W. Poel, A. Zakharova, and E. Schöll, Partial synchronization and partial amplitude death in mesoscale network motifs, *Phys. Rev. E* **91**, 022915 (2015).
- [24] Q. Wang, M. Perc, Z. Duan, and G. Chen, Synchronization transitions on scale-free neuronal networks due to finite information transmission delays, *Phys. Rev. E* **80**, 026206 (2009).
- [25] M. Ge, Y. Jia, Y. Xu, L. Lu, H. Wang, and Y. Zhao, Wave propagation and synchronization induced by chemical autapse in chain Hindmarsh–Rose neural network, *Appl. Math. Comput.* **352**, 136 (2019).
- [26] Y. Wu, Q. Ding, T. Li, D. Yu, and Y. Jia, Effect of temperature on synchronization of scale-free neuronal network, *Nonlinear Dyn.* **111**, 2693 (2023).
- [27] E. Yilmaz, M. Ozer, V. Baysal, and M. Perc, Autapse-induced multiple coherence resonance in single neurons and neuronal networks, *Sci. Rep.* **6**, 30914 (2016).
- [28] X. Hu, Y. Wu, Q. Ding, Y. Xie, Z. Ye, and Y. Jia, Synchronization of scale-free neuronal network with small-world property induced by spike-timing-dependent plasticity under time delay, *Physica D* **460**, 134091 (2024).
- [29] Y. Wu, Q. Ding, W. Huang, T. Li, D. Yu, and Y. Jia, Dynamic learning of synchronization in coupled nonlinear systems, *arXiv:2401.11691*.
- [30] Y. Wu, Q. Ding, W. Huang, X. Hu, Z. Ye, and Y. Jia, Dynamic modulation of external excitation enhance synchronization in complex neuronal network, *Chaos, Solitons Fractals.* **183**, 114896 (2024).
- [31] Q. Ding, Y. Wu, W. Huang, and Y. Jia, A dynamic learning method for phase synchronization control in Hodgkin–Huxley neuronal networks, *Eur. Phys. J. Spec. Top.* (2024), doi:10.1140/epjs/s11734-024-01171-w.
- [32] G. Petri, P. Expert, F. Turkheimer, R. Carhart-Harris, D. Nutt, P. J. Hellyer, and F. Vaccarino, Homological scaffolds of brain functional networks, *J. R. Soc. Interface.* **11**, 20140873 (2014).
- [33] S. Mirzaei, M. Mehrabbeik, K. Rajagopal, S. Jafari, and G. Chen, Synchronization of a higher-order network of Rulkov maps, *Chaos* **32**, 123133 (2022).
- [34] F. Parastesh, M. Mehrabbeik, K. Rajagopal, S. Jafari, and M. Perc, Synchronization in Hindmarsh–Rose neurons subject to higher-order interactions, *Chaos* **32**, 013125 (2022).
- [35] P. S. Skardal, L. Arola-Fernández, D. Taylor, and A. Arenas, Higher-order interactions can better optimize network synchronization, *Phys. Rev. Res.* **3**, 043193 (2021).
- [36] A. L. Hodgkin and A. F. Huxley, A quantitative description of membrane current and its application to conduction and excitation in nerve, *J. Physiol.* **117**, 500 (1952).

- [37] T. Li, D. Yu, Y. Wu, Q. Ding, and Y. Jia, Stochastic resonance in the small-world networks with higher order neural motifs interactions, *Eur. Phys. J. Spec. Top.* **233**, 797 (2024).
- [38] P. Erdős and A. Rényi, On random graphs I, *Publ. Math. (Debrecen)* **6**, 290 (1959).
- [39] D. J. Watts and S. H. Strogatz, Collective dynamics of ‘small-world’ networks, *Nature (London)* **393**, 440 (1998).
- [40] A. L. Barabási and R. Albert, Emergence of scaling in random networks, *Science* **286**, 509 (1999).
- [41] Y. Zou and G. Chen, Choosing effective controlled nodes for scale-free network synchronization, *Phys. A* **388**, 2931 (2009).